ChemComm

HIGHLIGHT

Check for updates

Advances in chemistry of CALF-20, a metal–organic framework for industrial gas applications

Joanna Drwęska, [iD] Kornel Roztocki [iD] * and Agnieszka M. Janiak [iD] *

The metal–organic framework CALF-20 is a super-stable adsorbent utilised for carbon dioxide capture and storage in cement plants. Furthermore, recent findings suggest its potential for various gas-related applications. In this brief review, we summarise ten years of research on CALF-20, emphasising its historical background and key findings. We discuss its flexibility, stability, processability, and tunability, detailing how these properties contribute to advancements in CALF-20 chemistry. We believe that this information will provide a better understanding of CALF-20 and assist in evaluating the potential of both novel and existing materials for gas-related applications.

Introduction

The most pressing concern facing the modern world is climate change, a phenomenon that poses significant challenges to ecosystems, economies, and societies worldwide.[1–3] Its origins can be traced back to the Industrial Revolution, which coincided with the beginning of the Anthropocene,[4] when the widespread use of fossil fuels, such as coal, oil, and natural gas, began to dominate energy production and consumption. This marked the onset of significant increases in greenhouse gas concentrations, particularly carbon dioxide. In July 2024, CO_2 has reached unprecedented levels of 426 ppm,[5] primarily due to human activities such as fossil fuel combustion and deforestation. In 2023, the burning of fossil fuels for energy, transportation, and electricity released a new record high of 37.4 billion tonnes of CO_2 into the atmosphere,[6] while intense deforestation for agriculture and urban development has reduced the planet's capacity to absorb carbon dioxide, further exacerbating the issue.[7]

As a consequence, the Earth's average temperature in 2023 has risen by 1.36 degrees Celsius compared to preindustrial times,[8] leading to a cascade of environmental impacts. These include more frequent and severe weather events such as hurricanes, droughts, and floods, alongside rising sea levels that threaten coastal communities.[9] The consequences for humans are profound: food security[10] is increasingly jeopardised by shifting agricultural conditions, access to clean water becomes strained, and public health risks rise due to an increase in heat-related illnesses[11] and the spread of infectious diseases.[12] Vulnerable populations, particularly in developing countries, are often the hardest hit, facing displacement and economic instability.

Effectively addressing this pressing issue requires not only limiting CO_2 emissions but also developing and implementing effective carbon capture technologies that can significantly reduce the amount of carbon released into the atmosphere.[13,14] Current strategies for CO_2 mitigation and negative emission include: (i) transitioning to renewable energy sources as solar, wind, hydro, *etc*.; (ii) improving energy efficiency; and (iii) developing/creating innovative materials capable of selectively capturing and storing CO_2. Among these, the application of solid adsorbent materials is widely regarded as a promising research direction, offering substantial benefits including considerably high CO_2 uptake efficiency, material stability, relatively easy regeneration and fabrication potential, and a wide process operability range.[15]

Generally, various classes of solid materials are under investigation for CO_2 capture,[16] including carbon-based materials, zeolites, polymers, silica, alumina, metal oxides, amine-based adsorbents and other porous materials such as metal–organic frameworks (MOFs). MOFs, in particular, have garnered attention for their high surface area, which provides numerous sites for CO_2 molecules, tunability, porosity, chemical affinity, reversibility, structure diversity, and low energy requirement for regeneration.[17] However, the industrial applicability of MOFs is often limited by their cost, poor processability, and insufficient thermal and chemical stability under real-world conditions. A notable exception is CALF-20 (Calgary Framework 20), a hydrophobic MOF that exhibits good CO_2 sorption capabilities in the presence of humidity.[18] One of the most remarkable attributes of CALF-20 is its impressive durability; it has demonstrated the ability to withstand up to 450 000 sorption cycles in steam.[18]

*Faculty of Chemistry, Adam Mickiewicz University, 61-614 Poznań, Poland.
E-mail: kornel.roztocki@amu.edu.pl, agnieszk@amu.edu.pl*

This resilience not only confirms its applicability for long-term use but also highlights its potential for integration into existing industrial processes that require continuous carbon capture and release. In addition, this material is easily scalable, which facilitates its swift adoption for industrial applications. Remarkably, CALF-20 is now produced at a multi-ton scale by Svante and is used as an effective CO_2 sorbent for carbon capture and storage (CCS) in cement plants.[19]

Given the recent surge of scientific interest in CALF-20 chemistry (evidenced by over thirty papers published since 2021 in the Web of Science database) and its applicability in various gas-related applications, we have highlighted the last ten years of research on this material. Point by point, we outline its historical background and discuss recent findings concerning the flexibility, stability, processability, and tunability of CALF-20. We believe that this information will contribute to a better understanding of the advancements in CALF-20 and assist in evaluating the potential of both novel and existing materials for gas-related applications.

General information about CALF-20

CALF-20 garnered widespread interest in the scientific community after it was reported by the George Shimizu group in their 2021 *Science* paper.[18] However, this was not the first report on CALF-20 from this group, as they initially described its synthesis and structure in a 2014 patent.[20] Moreover, they also developed and patented a large-scale synthetic procedure for the MOF five years later.[21] Nevertheless, the first scientific paper on a framework built from zinc(II), oxalate (ox), and triazolate (trz) ions was published by Wei and coworkers in 2016.[22] For the sake of clarity, we will refer to all reports on this MOF, including those published before the *Science* paper, as CALF-20.

This three-dimensional MOF with the formula of $[Zn(ox)_{0.5}(trz)\cdot0.25H_2O]$ was synthesised in a solvothermal reaction involving 1,2,4-triazole, oxalate, and zinc acetate in a water : acetonitrile mixture. Heating the mixture at 120 °C for five days yielded colourless block crystals. Further optimisation of the synthetic procedure increased the reaction temperature from 120 to 180 °C, while the reaction time was reduced to 48 hours. The oxalate ion is generated *in situ* from 2,5-dihydroxybenzoquinone added along with the remaining reagents to a 50% ethanol solution.[18] Conversely, the bulk synthesis utilises zinc oxalate and triazole dissolved in pure methanol. It is worth noting that mixing the same reagents with sodium fluoride and dissolving them in water, followed by heating for a week at 180 °C, resulted in a framework with the formula of $[Zn_2(ox)(trz)_2(H_2O)\cdot2H_2O]$ exhibiting the same connectivity as CALF-20, but with an additional water molecule ligated to each zinc ion.[23] Recently, Higuchi *et al.* reported a new way to obtain CALF-20 under ambient conditions.[24] By stirring zinc acetate with sodium oxalate in an aqueous methanol solution, followed by the addition of triazole, CALF-20 powder was obtained in just six minutes.
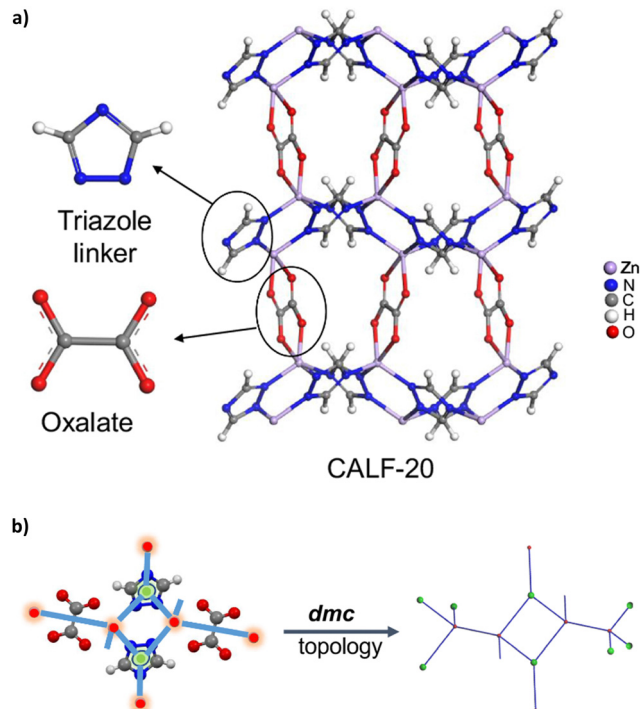

Fig. 1 (a) A graphical representation of the crystal structure of the CALF-20 framework along the *c* axis, highlighting the zinc–triazolate corrugated layers linked by oxalate ions. (b) A simplification of the 3D framework showing its **dmc** topology. Adapted with permission from ref. 25. Copyright 2024, Springer Nature.

Single-crystal X-ray diffraction (SC-XRD) experiments revealed that each zinc atom is five-coordinated (Fig. 1a).[25] The coordination sphere assumes a distorted trigonal bipyramidal shape and consists of three nitrogen atoms from three distinct trz anions as well as two oxygen atoms from one ox anion. Neighbouring zinc cations connected by nitrogen atoms at the 1- and 2-positions in the trz linker form Zn–N–N–Zn–N–N dinuclear units. The nitrogen atom at the 4-position connects the units into corrugated layers, which are further linked by the ox ligand into a 3D framework crystallising in the monoclinic space group $P2_1/c$ and exhibiting a **dmc** topology (Fig. 1b). The two-dimensional set of channels within the framework reaches 39.7% of the unit cell volume.

Sorption and separation capabilities of CALF-20

CALF-20 sorption properties

CALF-20 is now considered a benchmark MOF for CO_2 capture purposes owing to its remarkable gas sorption capacities. The Langmuir surface area calculated based on N_2 sorption data is 528 m^2 g^{-1} at 77 K. It was later determined that the adsorption isotherm can be described using the single-site Langmuir model.[26] CALF-20 exhibits a CO_2 uptake of 4.07 mmol g^{-1} at 1.2 bar and 293 K with the calculated heat of adsorption of -39 kJ mol^{-1}. Contrary to the N_2 curve, the type I

CO_2 adsorption isotherm fits the dual-site Langmuir model (Fig. 2a).

Understanding the sorption capacities of a material can be facilitated by an analysis of guest binding in the framework. Lin and coworkers applied grand canonical Monte Carlo (GCMC) and density functional theory (DFT) simulations to predict CO_2 binding sites. They proposed the middle of the pore as the most probable position of CO_2 molecules, with the shortest framework–guest distance of 3.03 Å forming between an oxygen atom from CO_2 and a hydrogen atom in the triazolate. According to their calculations, CO_2–MOF interactions are mostly of the attractive dispersion character (85%). The binding sites of CO_2 have also been the subjects of other studies. For example, first-principles calculations on the optimised structure of CALF-20, implemented by Roy and coworkers, confirmed the above-mentioned predictions.[30] Chen et al. used radial distribution functions (RDFs) to study MOF–guest interactions at the lowest loading.[31] They found that the CO_2 molecule can remain in close proximity to one oxalate ion, as indicated by O_{ox}–O_{ox} distances ranging from 7.0 to 8.1 Å. Finally, a study addressing the experimentally determined CO_2 positions in the framework was published.[32] Loading CO_2 into an activated CALF-20 single crystal at 10 bar and a subsequent in situ X-ray diffraction experiment revealed slight changes of the unit cell parameters induced by gas: while the b parameter expanded from 9.7321(1) to 9.8435(3) Å, the c parameter shrank from 9.5429(2) to 9.4623(3) Å. The CO_2 occupancy, estimated to be 0.45 molecules per asymmetric unit (ASU), indicates partial saturation of the crystal with carbon dioxide, compared to the calculated maximum uptake of 0.89 CO_2 molecules per ASU at 10 bar. The CO_2 molecule is oriented perpendicular to the oxalate. Surprisingly, neither of these sites corresponds to the positions indicated in the previously mentioned studies. Furthermore, the shortest distances between CO_2 and ox ions measuring 2.96(3) to 3.05(2) Å suggest the existence of electrostatic guest–MOF interactions between them.

Compared to other well-known CO_2 adsorbents, CALF-20 exhibits unusually low water uptake at low pressures, displaying a type V isotherm[18] with a clearly visible S-shape up to 30 °C (Fig. 2a). The isotherm is described by the cubic-Langmuir model.[28] The steep increase in the H_2O uptake only appears at ~10% relative humidity (RH); prior to that, the framework barely adsorbs any water. At ~15% RH, an inflection point is observed. The increase in adsorption capacity continues until ~30% RH, with a saturation capacity of ~8 mmol g^{-1}. However, other studies have reported even higher uptakes reaching ~1133 and ~15 mmol g^{-1}.[34] The Svante VeloxoTherm temperature swing adsorption (TSA) process used to regenerate CALF-20 on an industrial scale involves exposing the material to steam. However, studies on the equilibrium of water vapour at temperatures above 100 °C are still scarce. Consequently, Wilkins and coworkers developed a microscale dynamic column breakthrough (DCB) system capable of quantifying single-component steam (with N_2 as the balance) adsorption and tested pristine CALF-20 among other adsorbents in this system.[35] The experiments were carried out at ~0.97 bar and 110 °C.

Surprisingly, the inflection point shifts to a higher relative pressure between ~0.3 and ~0.48 bar in the steam experiment compared to the isotherm measured for CALF-20 at 22 °C.[18] This is an important observation in light of the utilisation conditions of CALF-20 since it highlights the possibility of an altered material behaviour at high temperatures in the presence of humidity. Hastings et al. measured steam adsorption at even higher temperatures (25–175 °C)[34] and noted a significant shift in the isotherm occurring after heating from 25 to 45 °C.

CALF-20 has also been studied as a potential hydrogen storage agent. Sutton and coworkers carried out a series of H_2 sorption experiments at low pressures and cryogenic as well as near-ambient temperatures,[36] revealing that the hydrogen uptake capacity of this material reaches 20.5 g L^{-1} at 1 bar and 77 K. This value situates CALF-20 among the top 10% of MOFs with a similar surface area. However, the H_2 uptake decreases significantly at 298 K, measuring only 0.69 g L^{-1}. GCMC simulations were performed to determine the performance of the material under real-world working conditions: at 5 bar and temperatures ranging from −50 to 50 °C. The working capacity of CALF-20 measures 10.5 g L^{-1}, which is significantly below the US Department of Energy target of 50 g L^{-1}.

In their recent report, Borzehandani et al. indicate that it is crucial to estimate the surface polarity of the adsorbent to understand its affinity for polar and non-polar gases.[37] Thus, they performed GCMC and molecular dynamics (MD) calculations to study the adsorption and mobility of two polar (hydrogen sulphide, sulphur dioxide) and two non-polar (fluorine, chlorine) adsorbates in CALF-20. Interestingly, the calculated adsorption isotherms showed that SO_2 and Cl_2 reach the saturation point at 3 mmol g^{-1} at 293 K and nearly zero gas pressure, indicating that their sorption process requires less energy than that of CO_2 which necessitates higher pressures. This phenomenon may be attributed to better fit of micropores in the CALF-20 framework for SO_2 and Cl_2 rather than for CO_2. The adsorption of H_2S is much lower than that of the previously mentioned compounds, while F_2 shows hardly any uptake. The RDF data corroborate these findings, indicating the level of guest distribution inside the pores in the order of F_2 < H_2S < Cl_2 < SO_2. The highest heat of adsorption of 45.51 kJ mol^{-1} for SO_2 suggests that, among all the gases studied, sulphur dioxide forms the strongest guest–MOF interactions. The mean square displacement calculations revealed that Cl_2 and SO_2 move through the framework at the slowest pace, while F_2 flows freely throughout the pores. The authors conclude that this is due to the lack of charge in the gas, resulting in an insufficient number of contact surfaces with the MOF.

CO_2 sorption of CALF-20 in the presence of water

Flue gas in cement plants contains water. Thus, it is important for the sorbent used to capture carbon dioxide to show resistance to humidity, preferably maintaining its CO_2 uptake capacity. Unfortunately, most MOFs exhibit decreased CO_2 uptake in the presence of water. In the case of CALF-20, however, CO_2 loading remains stable at humidity levels up to
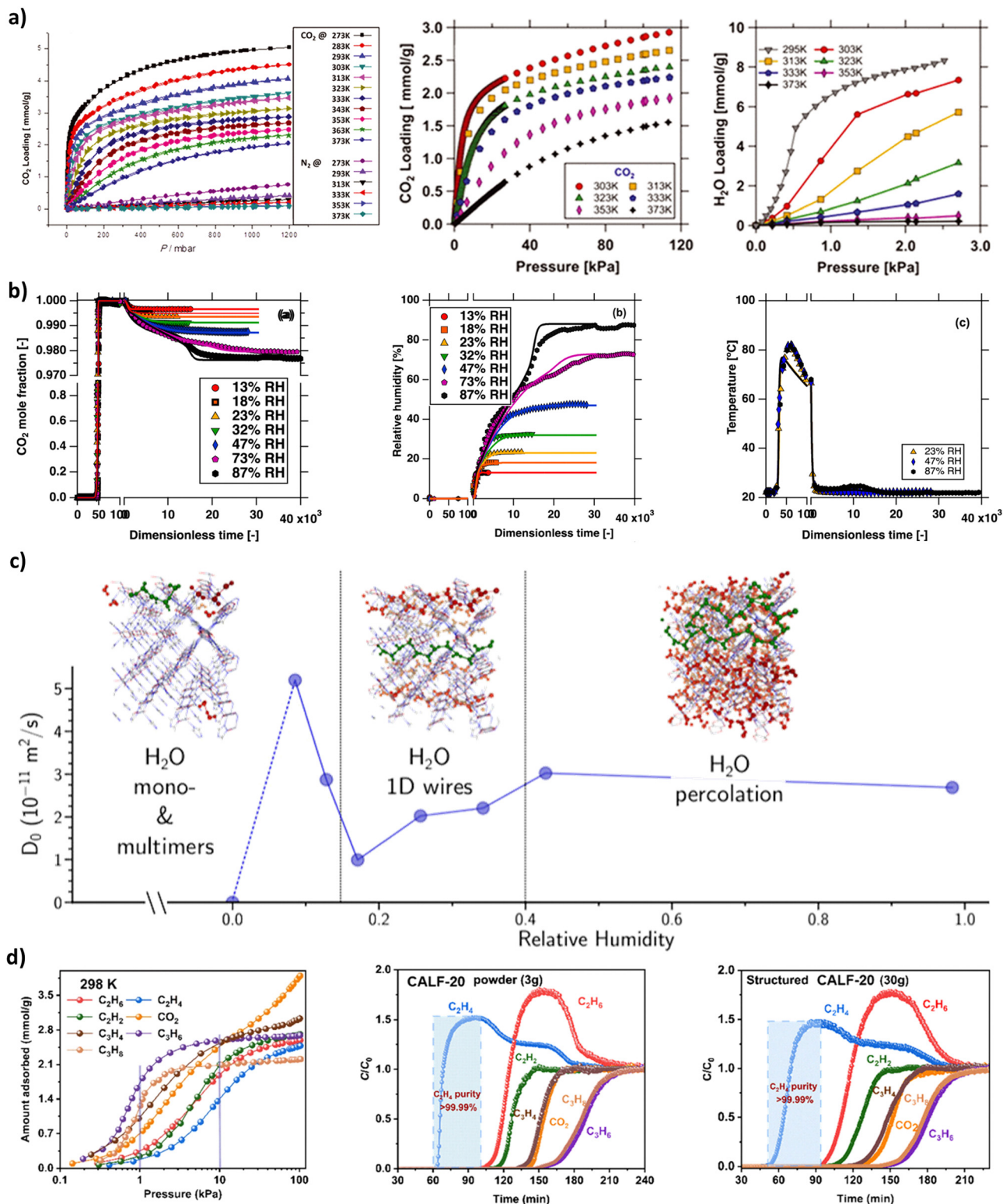
Fig. 2 (a) CO_2 and N_2 isotherms at 273–373 K measured for pristine CALF-20 (left), CO_2 isotherm at 303–373 K (centre), and water isotherm at 295–373 K (right) measured for structured CALF-20 (80% MOF, 20% polysulfone). Adapted with permission from ref. 18. Copyright 2021, AAAS. (b) Competitive breakthrough curves of CO_2 (left) and water (centre) at 13–87% RH, 0.97 bar, and 22 °C, and column temperature history (left). Adapted with permission from ref. 28. Copyright 2024, ACS. (c) Changes in the diffusion coefficient in rising relative humidity with a graphical representation of corresponding self-association motifs created by adsorbed water molecules. Adapted with permission from ref. 40. Copyright 2023, ACS. (d) C_2H_2, C_2H_4, C_2H_6, CO_2, C_3H_4, C_3H_6, and C_3H_8 adsorption isotherms at 298 K measured for pristine CALF-20 (left), and breakthrough curves of a seven-component mixture on pristine (centre) and structured (90% MOF, 10% cellulose; right) CALF-20. Adapted from ref. 45. Copyright 2024, CCS.

20% RH, as proven by DCB studies (Fig. 2b).[18,28] The competition between CO_2 and H_2O becomes noticeable beyond 20% RH. Nevertheless, the decrease in the CO_2 sorption capacity of CALF-20 is relatively small, and the MOF still adsorbs over 2 mmol g^{-1} of carbon dioxide up to 50% RH. Then, the gas uptake shows a significant drop, followed by a complete loss of CO_2 sorption capacity beyond 70% RH. Nonetheless, CALF-20 remains the most effective physisorbent in terms of CO_2 sorption performance in the presence of water.[38]

Moreover, the presence of CO_2 also changes the H_2O adsorption capacity of CALF-20. The shift in the water adsorption isotherm with CO_2 present indicates that carbon dioxide hinders the H_2O uptake in CALF-20. According to the simulations, the framework adsorbs 6 mmol g^{-1} of water at 20% RH without CO_2, but with CO_2 present, it only reaches this value at 40% RH.

The higher affinity of CALF-20 for CO_2 is also confirmed by the values of isosteric heats of adsorption at low water loadings (below 2 mmol g^{-1}) reaching ~ 35 kJ mol^{-1} for H_2O and ~ 39 kJ mol^{-1} for CO_2. However, the heat of adsorption of water increases with increasing H_2O loading, indicating stronger interactions between water molecules.

Nguyen and coworkers measured competitive loadings in CO_2 + H_2O DCB experiments carried out on CALF-20 structured with polysulfone at 0.97 bar and 22 °C with relative humidity ranging from 13 to 90%.[28] Regardless of the RH, CO_2 consistently eluted at a dimensionless time of ~ 47, while water was only detectable at ~ 400. Between 13 and 47% RH, the CO_2 concentration decreased steadily, while it reduced more rapidly between 73 and 87% RH. The authors concluded that the competitive CO_2 adsorption process may be described by the modified Langmuir model.

A theoretical study of CO_2/H_2O competitive adsorption on a molecular level was carried out by Ho and Paesani.[39] They employed MD simulations with data-driven many-body potential energy functions owing to their ability to correctly predict the behaviour of water and carbon dioxide under various conditions. The RDF data simulated for both guest molecules separately suggested that preferential binding sites for both carbon dioxide and water are located close to the oxalate ions. The authors imply that a framework with less polarised charge distributions may show a higher affinity for CO_2 than for H_2O. This could be realised through the presence of metal centres in low oxidation states and ligands containing atoms with low electronegativity. RDFs of CO_2 + H_2O mixtures under ambient conditions revealed a mutual volume exclusion of these compounds. Moreover, both of them form long-range order structural patterns. The subsequent analysis of the volume exclusion phenomena through MD simulations of the mixtures under various humidities indicated that between 27.5 and 59.7% RH, water molecules self-associate into networks connected by hydrogen bonds. This behaviour may be due to CO_2 molecules pushing water molecules into less favourable positions, thereby forcing them to be located closer together, which results in the formation of networks. The presence of H_2O networks in the framework causes the CO_2 adsorption to be more energetically favourable than in the absence of water.

The competition between carbon dioxide and water for the same binding sites leads to faster reorientation dynamics of CO_2. Finally, H_2O entropy is more sensitive to CO_2 because of the increase in the number of $H_2O–H_2O$ interactions, while CO_2 entropy is only influenced by water at high RH, when more void space is already occupied by H_2O molecules. Similar conclusions were drawn by Magnin et al. (Fig. 2c).[40] Additionally, they discovered that at a CO_2 pressure of 0.1 bar, the carbon dioxide adsorption drops abruptly at $\sim 42\%$ RH, suggesting an effective way for CO_2 desorption at moderate partial pressures using humidity.

Several reports concerning CO_2/H_2O sorption capabilities of CALF-20 have used IAST to understand and quantify data obtained experimentally. However, Krishna and van Baten implied that IAST estimates deviate from the experimental observations.[27] Under low humidity conditions, IAST tends to underestimate CO_2 uptake, whereas at high RH, the CO_2 sorption capacities of the framework are overestimated. In order to explain this phenomenon, they applied conformational bias Monte Carlo calculations and RDFs. Based on the theoretical data, it can be established that at low RH, CO_2 and H_2O segregate within the pores (which is in agreement with the observations from the previously described reports[39,40]), while IAST assumes a homogenous distribution of both compounds throughout the material. The lack of direct competition between the adsorbates under these conditions leads to an underestimation of the CO_2 loading in CALF-20. At high RH, carbon dioxide and water compete for the same binding sites. Furthermore, water molecules are connected into a hydrogen-bonded network. Thus, the level of competition is significantly higher than IAST predicts, leading to an overestimation of CO_2 sorption capacity. The same trends apply to methane adsorption and are explained by the same phenomena.[41]

CALF-20 separation properties

CALF-20 was initially tested for CO_2/N_2 selectivity. Lin et al. utilised ideal adsorbed solution theory (IAST) to calculate the selectivity coefficient, which reached 230 for a CO_2/N_2 mixture with a 10:90 ratio.[18] The first DCB studies performed on CALF-20 structured with polysulfone confirmed trends indicated by single-component isotherms. While N_2 eluted through early on, at a dimensionless time of ~ 4, CO_2 was detected much later (dimensionless time of ~ 700 for a mixture with 5% CO_2 content). The breakthrough time for CO_2 decreased along with the increase of the CO_2 content in the mixture. On the other hand, Nguyen and coworkers studying the CO_2/N_2 adsorption competitiveness[26,42] concluded that the behaviour could be predicted using the extended dual-site Langmuir model with an equal energy site approach. Computational optimisation of the separation process using a four-step vacuum swing adsorption with light product pressurization configuration indicated that CALF-20 should be capable of producing CO_2 with 95% purity and 90% recovery. Indeed, the experiments resulted in 95.5% purity and 88.1% recovery. In another report by Peh et al., a simulation of a four-step TSA cycle showed that the productivity of CALF-20 depends on the feed velocity.[43]

Once the velocity surpasses the fluidization limit, a notable increase in productivity is observed without a pressure drop. A velocity of 12 m s^{-1} allows for retention of 88.7% purity and 82.7% recovery.

CALF-20 has also been proposed as a potential candidate for separation of CO_2 from acetylene.[33] Single-component adsorption experiments carried out at 1 bar and 298 K showed that the material adsorbs CO_2 much more readily than C_2H_2, with adsorption capacities of 140.2 and 102.6 cm^3 cm^{-3}, respectively. The selectivity calculated using IAST for a 50 : 50 CO_2/C_2H_2 mixture is 2.7. The estimated heats of adsorption at zero loading (37.7 kJ mol^{-1} and 33.8 kJ mol^{-1} for CO_2 and C_2H_2, respectively) match the experimental observations. Nevertheless, the study lacks the analysis of CO_2/C_2H_2 competitive adsorption, whether experimental or theoretical.

J. Peng and coworkers[44] evaluated the role of CALF-20 in the separation process of propene (C_3H_6) and propane (C_3H_8). Equilibrium uptake capacity measured at 650 torr and 363 K is 76 mg g^{-1} for both adsorbates; however, their equilibrium times differ significantly, with 25 min for propene and 1000 min for propane. The relatively low heat of adsorption for propene at zero loading of ~ 43 kJ mol^{-1} suggests that these gases can be separated kinetically. The framework exhibits the highest propene/propane selectivity, reaching 1565 at 323 K.

X. Peng *et al.* examined the ability of CALF-20 to purify ethylene from a seven-component cracking gas mixture (Fig. 2d).[45] Unary adsorption experiments confirmed that the framework exhibits the lowest affinity for C_2H_4 in the CO_2/C_2H_2/C_2H_4/C_2H_6/C_3H_4/C_3H_6/C_3H_8 mixture. It is worth noting that, unlike most adsorbents, CALF-20 can effectively adsorb CO_2, C_2H_6, and C_2H_2 even at lower pressures, corresponding to the composition of real cracking gas. The material also displays high selectivity for other components over C_2H_4. Breakthrough tests revealed the possibility of collecting polymer-grade ($> 99.99\%$) ethylene with a productivity of 19.8 L kg^{-1}. Importantly, CALF-20 does not exhibit any loss of its purification capacity even at high humidity (74% RH). SC-XRD experiments paired with molecular simulations confirmed that the guest binding induces slight structural transformations in order to maximise the MOF–guest interactions.

CALF-20 has also been proven to effectively separate *n*-butene from isobutene through a temperature-controlled sieving process involving structural adjustments facilitating the separation and increasing the selectivity.[46] At 1 bar and 298 K, the material adsorbs as much as 2.62 mmol g^{-1} of *n*-C_4H_8, which is the highest value reported to date. In contrast, the iso-C_4H_8 uptake under the same conditions reaches only 0.178 mmol g^{-1}. Intriguingly, the *n*-C_4H_8 uptake does not decrease until 373 K, unlike most materials tested for separating butene isomers. Meanwhile, the iso-C_4H_8 uptake decreases with increasing temperature, a phenomenon that can be used to manipulate the separation process. Minimum energy path calculations indicated that as temperature increases, the diffusion rate of *n*-butene also increases, thus facilitating the penetration of *n*-C_4H_8 molecules into the framework. Isobutene, in turn, faces a higher energy barrier of 158 kJ mol^{-1} and cannot move as freely in the narrow

pores of CALF-20. DCB experiments yielded high-purity (99.5%) iso-C_4H_8, which eluted almost instantly, while *n*-butene was only detected after 60 minutes. Notably, the separation process was not hindered by humidity. These findings were corroborated by another study conducted by Jiang and coworkers, who achieved an even higher purity of 99.999% for isobutene.[29] Moreover, *in situ* SC-XRD studies of gas-loaded CALF-20 indicated the real positions of *n*-butene within the framework. It was found to occupy centres of two different sites where it forms hydrogen bonds with the oxalate ligands. The C–H···O and C–H···C bond lengths range from 2.267 to 3.034 Å. Interestingly, the accommodation of *n*-C_4H_8 triggers a slight deformation of the CALF-20 framework.

Yu *et al.* investigated the uptake capacities of noble gases in CALF-20.[47] The adsorption isotherms of xenon measured at 278–298 K exhibit a type I shape, revealing the physical nature of the sorption process, whereas the krypton isotherm is nearly linear. The heat of adsorption calculated for Xe is over twice as high as that for Kr (29 kJ mol^{-1} and 14 kJ mol^{-1}, respectively). Both these characteristics indicate a stronger affinity of the framework for Xe than for Kr. This is corroborated by the value of Xe/Kr selectivity calculated based on Henry's constants and found to be 12.5. Additionally, breakthrough experiments carried out for a Xe 20 : 80 Kr mixture show that Kr leaves the column within the first minute, while Xe does not elute until four minutes and only reaches feed concentration after ten minutes. Interestingly, three years after the abovementioned report, a similar study on CALF-20 was conducted by Wei and coworkers.[48] Based on adsorption data recorded for Xe, Kr, and N_2, they determined the maximum uptake of Xe and Kr at 1 bar and 298 K to be 2.45 mmol g^{-1} and 1.12 mmol g^{-1}, respectively. The selectivity calculated in the same manner as described above measures as high as 13.2, matching that of many other MOFs utilised for noble gas separation. DCB studies corroborated the findings from the earlier report. Moreover, the authors calculated the Xe working capacity to be 0.65 mmol mL^{-1}.

Structural changes and stability of CALF-20

To date, CALF-20 has demonstrated exceptional stability under various conditions, including exposure to steam and acid gases.[18] Fan *et al.* decided to extend the knowledge on the framework by gaining insight into its mechanical and thermal properties using DFT and machine learning potential molecular dynamics (MLP-MD) simulations.[49] A tensor-based analysis carried out at 0 K showed that CALF-20 exhibits a rare negative area compressibility (NAC) behaviour evidenced by a shrinking of the *c* axis with concomitant lengthening of the *a* and *b* axes while the framework is compressed. This phenomenon may cause CALF-20 to be an interesting candidate for mechanical sensing purposes. The predicted Young's modulus and Poisson's ratio show high anisotropy and suggest greater durability of the framework along the *a* axis, parallel to the oxalate linkers, whereas the Zn-triazolate layers exhibit higher flexibility. While mechanical pressure is applied, the material shows similar

behaviour, with the strain tensor eigenvector along the a axis reaching up to $-188.77\ TPa^{-1}$.

Notably, a rare biaxial negative linear compressibility phenomenon is also observed in CALF-20 crystals. However, no structural collapse occurs even at pressures up to 1 GPa. Above that value, a pressure-induced structural transformation occurs, leading to a metastable, non-porous phase with a high density of $3.58\ g\ cm^{-3}$. Interestingly, at room temperature, another transformation occurs between 0.3 and 0.4 GPa, during which the b and c axes change more than the a axis.

The investigation of the thermal properties of CALF-20 revealed that the framework exhibits negative thermal expansion (NTE) behaviour at low temperatures. The thermal expansion coefficient reaches its lowest value of $-10.56\ MK^{-1}$ at 40 K. Small changes of the unit cell volume at variable temperatures also confirm the flexibility of the material. The MLP-MD simulations applied to assess thermal properties at higher temperatures showed a continuous decrease in the b axis with increasing temperature, thereby confirming the NTE phenomenon, as evidenced by the thermal expansion coefficients ranging from -4.22 to $-60.81\ MK^{-1}$. The latter value is considerably higher than those reported for other typical MOFs exhibiting NTE behaviour, e.g. DUT-49 ($-32.778\ MK^{-1}$). This suggests that CALF-20 may also be utilised as a thermal sensor.

The deformation behaviour of the material induced by an ideal tensile strain was also examined. CALF-20 exhibits remarkable integrity up to the strain level of 27% at room temperature, owing to the flexibility of the material resulting from the NAC and NTE behaviours. Additionally, it also demonstrates significant mechanical resilience. However, the stress–strain curve at 0 K revealed a possible phase transition corresponding to the peak at 18.43% when the tensile strain is applied along the c axis. The DFT optimisation suggested that the new phase is metastable and capable of readily returning to the original phase due to a minimal energy barrier for the reverse transition (0.03 eV per unit cell).

In order to fully understand the stability of CALF-20, it is essential to examine the influence of various external stimuli on the framework. A theoretical and experimental study conducted by Oktavian and coworkers in collaboration with Svante focused on investigating the impact of guest molecules on the structure of CALF-20.[25] Slight discrepancies between the powder X-ray diffraction (P-XRD) patterns of evacuated and ethanol-soaked powder samples indicated pore contraction and expansion between the Zn-trz layers upon evacuation of solvent molecules at 110 °C under N_2 flow (Fig. 3a). After exposure to CO_2 or soaking the sample in water, the layers contract again; however, no pore expansion is observed for the CO_2-loaded sample. Significant changes in the powder pattern were only noted for the sample exposed to >20% RH, indicating that CALF-20 reacts differently to water vapour than to soaking in liquid water. Additionally, this analysis suggests that the framework requires less structural adjustment to accommodate CO_2 than water, which may explain its higher affinity for the former compound.

The effect of humidity on CALF-20 was further investigated by Chen et al.[31] A three-day exposure of the activated CALF-20 powder to >23% RH at room temperature induces a structural transformation of the original phase (now dubbed α-CALF-20) into a new polymorph called β-CALF-20 (Fig. 3b). Interestingly, the unit cell parameters of this phase are nearly identical to those of the hypothetical phase predicted to form upon the application of tensile strain described earlier.[49] The Rietveld refinement of the P-XRD pattern supported by pair distribution function data revealed the possible structure of the novel phase. While it retains the symmetry and topology of α-CALF-20, its most notable feature is the altered coordination environment of the Zn centres, a result of the elongation followed by a breakage of one of the bonds between zinc and the oxalate ion. Thus, the coordination number of the metal cations decreases from five in α-CALF-20 to four in β-CALF-20. Furthermore, an adjustment in the positions of triazolate ligands is also observed. Consequently, the unit cell volume, and therefore the pore volume, decreases by $\sim 4.8\%$. The transformation is fully reversible within 15 minutes, even under a He flow. The sample experiences no loss of crystallinity. Because the reverse transformation occurs so readily, Chen and coworkers could not study the sorption properties of β-CALF-20 experimentally. Nevertheless, the simulations indicated a higher heat of CO_2 adsorption at zero loading for β-CALF-20 compared to α-CALF-20, which may be attributed to a smaller pore aperture in the former phase. It is worth noting that competitive CO_2/H_2O sorption experiments revealed that the phase transition has a negligible effect on the CO_2 sorption capacity of CALF-20.[34] However, the RDFs suggested that the pore geometry and the orientation of oxalate ligands in β-CALF-20 are more suitable for CO_2 uptake, as the guest molecule is in close proximity to two ox ligands instead of only one in α-CALF-20. Curiously, the authors note that a decrease in the coordination number in the presence of water is a rare occurrence as water tends to coordinate readily with open metal sites. They hypothesise that the phase transformation might be induced by the possibility to form hydrogen bonds by water molecules instead.

Recently, another phase transformation of CALF-20 was reported.[32] This time, it was triggered by temperature. Heating α-CALF-20 crystals in a convection oven for ten days at 80 °C resulted in a single-crystal-to-single-crystal transformation to γ-CALF-20 with the formula of $[Zn_2(ox)(trz)_2(H_2O)\cdot s]$ (s – solvent molecules) (Fig. 3b). Similarly to the α and β phases, γ-CALF-20 crystallises in the monoclinic space group $P2_1/c$ and displays the **dmc** topology. Nevertheless, the coordination sphere of statistically half the Zn centres contains an additional water molecule, thus increasing the coordination number from five to six. The remaining cations are still five-coordinated, but the coordination geometry changes from distorted trigonal bipyramidal to distorted square pyramidal. There is a pronounced decrease in void volume from 39.4% in α-CALF-20 to 11.7% in γ-CALF-20. Intriguingly, a shorter heating time of seven days under the same conditions triggers the formation of a structurally transient τ-CALF-20 phase (Fig. 3b). Its connectivity is identical to that in γ-CALF-20. The most significant difference between these two phases is the bond length between the zinc cation and the water molecule; this bond is longer in the
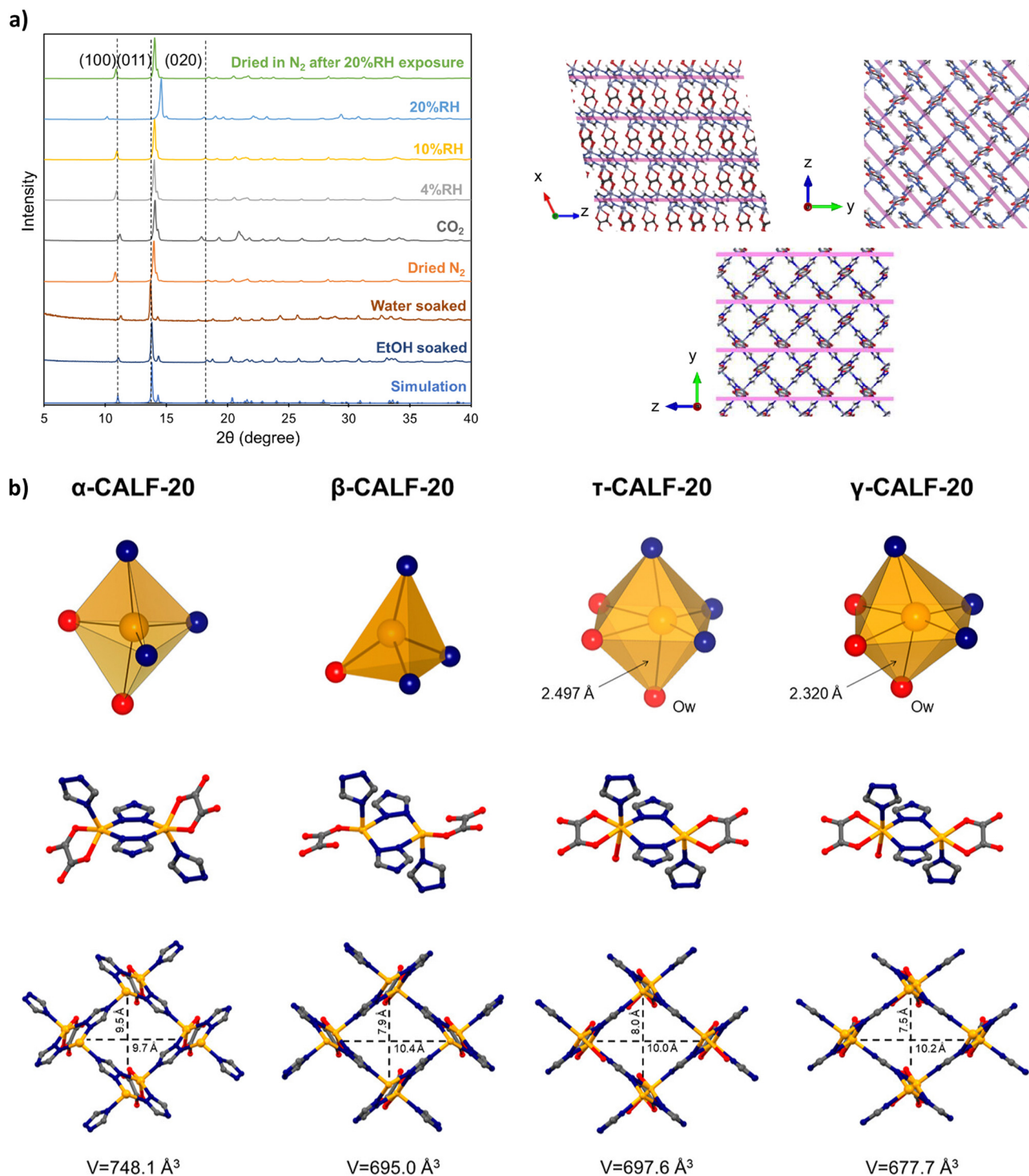
Fig. 3 (a) P-XRD patterns of CALF-20 powder exposed to various stimuli (left side) and visualisation of planes in the CALF-20 structure where the most prominent shifts were observed (right side): (100) – top left, (011) – top right, (020) – bottom. Adapted with permission from ref. 25. Copyright 2024, Springer Nature. (b) Structural comparison of all CALF-20 phases reported so far comprising shapes of coordination spheres (top row), coordination environments of zinc ions (middle row), and views of the frameworks along the *a* axis (bottom row). Adapted with permission from ref. 32. Copyright 2024, ACS.

τ phase (2.497 Å) than in the γ phase (2.320 Å). Remarkably, the powder pattern of τ-CALF-20 aligns perfectly with that of previously reported β-CALF-20[31] despite significant disparities between their structures. It is worth noting that the structure of τ-CALF-20 was derived from SC-XRD data, whereas β-CALF-20 was suggested based on the powder pattern. Additionally, the

geometry of β-CALF-20 is highly unusual. Chen *et al.* noted that a decrease of the coordination number of zinc centres in the presence of water is also a rare occurrence.[31] Based on these factors, we believe that τ-CALF-20 represents the correct description of the phase obtained by Chen and coworkers. Therefore, we will henceforth refer to β-CALF-20 as τ-CALF-20.

CO_2 sorption isotherms calculated for τ-CALF-20 and γ-CALF-20 suggested that both new phases exhibit lower CO_2 uptake than α-CALF-20 (2.5 mmol g^{-1} for τ-CALF-20 and 0.5 mmol g^{-1} for γ-CALF-20 at 1 bar). Theoretical calculations concerning the γ phase revealed that it is more stable in the presence of water than α-CALF-20. However, the existence of another, closed-pore δ-CALF-20 phase stable at very low temperatures has also been predicted.

Enhanced properties of CALF-20 hybrids

Metal–organic frameworks are often combined with other materials, commonly referred to as binders, to obtain composites exhibiting properties of both (or more) constituents or to enhance the properties of the MOF. Attempts to structuralise CALF-20 by mixing it with other materials have been made since the first report by Lin *et al.*, in which the MOF was combined with polysulfone (80% MOF) and retained the crystallinity of pristine CALF-20. Notably, the resulting composite exhibits excellent stability under real industrial conditions, as proven by its resilience to (i) 150 °C steam, (ii) gaseous SO_2 and NO_X at 20 °C, and (iii) real flue gas. It was also tested using the Svante VeloxoTherm regeneration process, thus confirming its industrial applicability. The potential for developing other composite materials featuring CALF-20 have been vastly explored, particularly in the context of creating membranes.

CALF-20 membranes

As mentioned before, CALF-20 exhibits stable CO_2 uptake capacities along with high selectivity over nitrogen even under humid conditions, which facilitates the use of this framework for capturing CO_2 from wet flue gas. Nevertheless, its morphology and relatively large particle size may hinder the CALF-20 incorporation into membranes. To address this issue, Jia and coworkers investigated the possibility of incorporating this MOF into a polymer matrix.[50] Since membranes made from pure polymers often do not offer satisfactory permeability and selectivity simultaneously, a creation of a mixed-matrix membrane (MMM) might result in obtaining a product with enhanced performance. Thus, CALF-20 was prepared in a nanoplatelet form using $Zn_5(OH)_8(NO_3)_2 \cdot 2H_2O$ as a layered precursor. Indeed, the microwave synthesis of CALF-20 involving the aforementioned compound resulted in thin plates of platelet morphology, dubbed CALF-20(P), with an estimated thickness of ∼30 nm. However, the analysis of the powder pattern of the initial product revealed that it was τ-CALF-20[31] that only transformed into the original α-CALF-20 phase upon evacuation. CALF-20(P) was then combined with the PEBAX

MH1657 polymer matrix, yielding ∼50 μm thick membranes with a 3–10% wt MOF content. Sorption experiments carried out at 1.2 bar and 293 K confirmed that adding CALF-20 into the membrane improves its permeability by 37% and CO_2/N_2 selectivity by 67% for MMMs with up to 7% wt. Even though the diffusivity of the membranes decreases compared to that of a pure PEBAX sample, the MMMs exhibit improved CO_2 solubility. CALF-20 has also been proven to enhance the CO_2 permeation of the membranes in the presence of humidity.

In their 2024 report, Zhang *et al.* note that the most relevant parameter for MMMs from the perspective of their industrial applicability is CO_2 permeability, especially at low pressures.[51] Permeability can be provided by polymers of intrinsic porosity (PIMs) such as PIM-1 built from rigid chains. However, the addition of CALF-20 into the membrane leads to a significant increase in its separation capacities. In this study, the MOF particle size was reduced by extensive ultrasonification and stirring. As little as 5% loading of the MOF increased the permeability of the 5%-CALF-20/PIM-1 membrane by 38.7% compared to a pure PIM-1 membrane (Fig. 4a). Moreover, CO_2/N_2 selectivity also showed a 25% improvement, thus surpassing the Robeson upper limit. The authors suggest that this enhancement could be due to a higher affinity for CO_2 by CALF-20 combined with the rigid microporous structure of PIM-1 allowing for ultrafast CO_2 transport throughout the membrane. Theoretical calculations indicated that the CO_2/N_2 solubility selectivity of 5%-CALF-20/PIM-1 reaches 27.41, while the diffusion selectivity equals 0.64.

The excellent attraction for CO_2 demonstrated by CALF-20 can also be applied in new engineering solutions for the electrocatalytic carbon dioxide reduction reaction (CO_2RR). This material was evaluated by Al-Attas *et al.* as a potential catalyst for the reduction of CO_2 to CO.[52] CALF-20 exhibits the highest selectivity towards the CO_2RR achieving a faradaic efficiency of 94.5% at −0.97 V *vs.* the reversible hydrogen electrode (RHE) with a turnover frequency reaching 1360.8 h^{-1}. However, its stability under cathodic potential is unsatisfactory. Based on these findings, the authors designed a permselective gas diffusion electrode (PGDE) capable of selectively capturing CO_2 from a diluted gas stream, followed by its immediate reduction using an Ag-based catalyst.[53] The electrode made of porous PTFE features a CO_2-selective MMM on one side and the catalyst on the other. The membrane consists of CALF-20 mixed with Nafion polymer to enhance its mechanical stability. The incorporation of the MOF improves the faradaic efficiency by ∼64% at −1.32 V *vs.* RHE compared to a pure Ag/PTFE. CALF-20 also circumvents the decrease of the electrochemical performance of the electrode caused by O_2, which does not permeate the membrane and thus does not reach the catalyst. Notably, the PGDE retains its faradaic efficiency under humid conditions.

Other CALF-20 composites

An approach to further improve the CO_2 sorption capacities of CALF-20 was proposed by Feng *et al.*[54] It involved an *in situ* crystallisation of the framework inside microporous poly(acrylate) beads. Similarly to the crystallisation of platelets mentioned
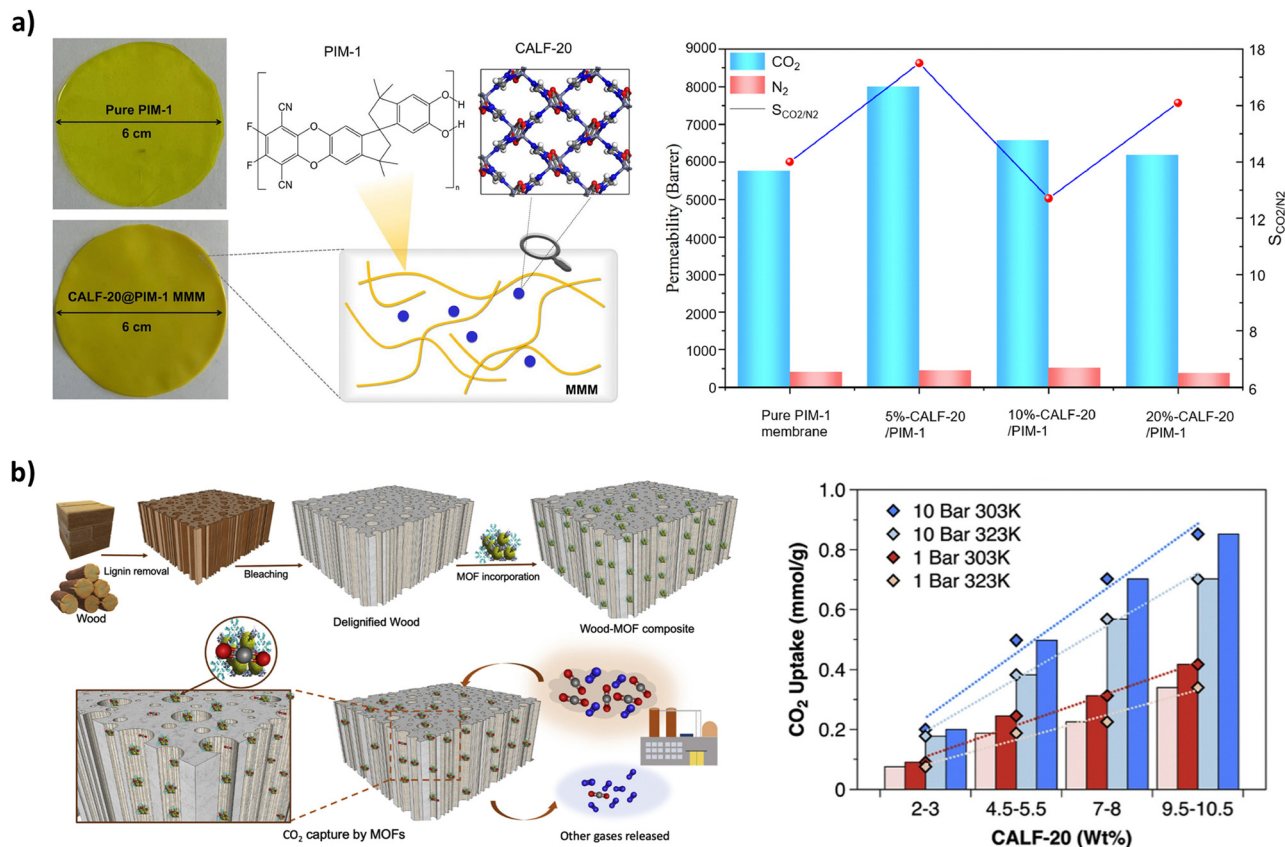
Fig. 4 (a) Comparison of a pure PIM-1 membrane to a mixed-matrix one along with a scheme depicting the composition of the latter (left) and a graphical representation of permeability (bars) and selectivity (points) of CALF-20/PIM-1 membranes (right). Adapted with permission from ref. 51. Copyright 2024, Elsevier. (b) Preparation scheme of the CALF-20 functional wood (left) and its CO_2 uptake capacity depending on the MOF loading measured at various pressures and temperatures (right). Adapted with permission from ref. 30. Copyright 2023, Cell Press.

earlier,[50] the P-XRD experiments confirmed the creation of τ-CALF-20. However, the activated sample transformed into α-CALF-20. This crystallisation technique yielded CALF-20 particles with an average size of ∼170 nm, representing a ten-fold decrease compared to particles that grew freely in solution (1.8 µm). The CO_2 adsorption capacity of the CALF-20@poly(acrylate) composite at 0.1 bar and 313 K is 2.78 mmol g^{-1}, meaning that its thermodynamic adsorption efficiency surpasses that of pristine CALF-20 by 32%. The sensitivity of the composite to temperature suggests it could be regenerated using the TSA process. Indeed, it was capable of retaining 94.9% of its initial CO_2 uptake after seven days under regeneration conditions. It is worth noting that CALF-20@poly(acrylate) appears to be resistant to humidity. Multicomponent adsorption experiments revealed a retention of 97.1% of the CO_2 uptake capacity of the composite at 90% RH and 313 K, and it was proven to be stable after ten CO_2 adsorption–desorption cycles. In addition, the composite shows resistance to SO_2. Interestingly, the synthetic procedure is easily scalable. Kilogram-grade CALF-20@poly(acrylate) exhibits a higher CO_2 adsorption capacity than CALF-20 structured with polysulfone (1.85 mmol g^{-1} vs. 1.65 mmol g^{-1} at 0.1 bar and 313 K, respectively).

Sedighi and coworkers opted for creating a CALF-20 composite with graphene oxide (GO) owing to its ability to enhance MOF stability and increase the number of active sites, resulting in improved gas diffusion into the framework.[55] Three CALF-20/GO composites with 10, 15, and 20% wt of GO were prepared. The GO content leads to a reduction in the IR spectra compared to pristine CALF-20. This may be attributed to the breakage of chemical bonds in the MOF. Notably, all composites exhibit a higher N_2 uptake than pristine CALF-20, suggesting their larger surface areas than the pure MOF. The more GO the material contains, the more N_2 it can adsorb. Specifically, CALF-20/GO-20 is capable of adsorbing 41.8% more N_2 compared to pure CALF-20. The same trend is observed in the CO_2 sorption capacity. Again, CALF-20/GO-20 displays the highest CO_2 uptake reaching 4.05 mmol g^{-1} at 1.6 bar and 298 K, which represents a 42.6% increase compared to the pristine MOF. The predicted CO_2/N_2 selectivity value of 282.26 at 1 bar constitutes a 32.7% improvement over pristine CALF-20. A simulation of dynamic breakthrough curves for a CO_2 15%:85% N_2 mixture revealed that CO_2 was detected after 168 min for CALF-20/GO-20, which is 37 min longer than that for CALF-20. Thus, the composite displays more favourable competitive CO_2/N_2 adsorption. Nevertheless, one disadvantage of CALF-20/GO-20 is its higher adsorption enthalpy compared to pure CALF-20. Additionally, the performance of the composite in the presence of humidity has not been tested yet.

Another interesting material for creating functional composites is wood. It combines biodegradability, modularity, porosity, and mechanical resilience, and it can be easily altered through chemical modification. Roy *et al.* proposed a CALF-20-incorporated wood displaying high CO_2/N_2 selectivity (Fig. 4b).[30] The repeatable preparation process comprises two steps: wood delignification and introduction of CALF-20 microparticles (ranging from 1 to 2 mm) into the pores of the wood, reaching up to 10% MOF loading. The resulting material, dubbed Wd-CALF-20, retains its structure. Furthermore, the addition of the MOF further strengthens the material, as proven by thermogravimetric analysis. Wd-CALF-20 is characterised by a type II N_2 isotherm, thus confirming the existence of both micro- and mesopores in the structure. The normalised CO_2 uptake calculated per gram of CALF-20 reaches 3.8 mmol g^{-1} at 1 bar and 323 K, surpassing that of the pristine MOF. However, it is comparable to pure CALF-20 at lower pressures, which suggests that the presence of mesopores in the wood improves the overall composite performance at ambient pressures. A study of the adsorption capacities of pristine CALF-20 at high pressures (up to 30 bar) revealed that the framework reaches saturation at 5 mmol g^{-1} at 1.2 bar. Conversely, Wd-CALF-20 exhibits an increase in CO_2 uptake directly proportional to the increase in pressure. At 30 bar and 273 K, the composite adsorbs 3.7 mmol g^{-1} owing to the meso- and macropores present in the structure. The DCB experiments carried out at 20% RH for CO_2/N_2 mixtures with less than 10% CO_2 content revealed improvements in both breakthrough time and the CO_2 uptake of the composite.

The implementation of MOF composites in real industrial processes requires precise control over the shaping of MOF particles in those materials. Inspired by this notion, Naskar and coworkers carried out a theoretical investigation of the influence of polymeric binders on the structuring of resulting composites and their CO_2/N_2 separation capacities.[56] The binders of choice were carboxymethyl cellulose (CMC), poly(vinyl acetate), poly(vinyl butyral), and poly(vinyl alcohol). According to the calculations, CMC exhibits the highest performance among all binders investigated. First, the CMC–CALF-20 composite demonstrates the strongest level of MOF–binder adhesion. This is attributed to (i) hydrogen bonds forming between the hydroxyl groups of the polymer and water molecules coordinated at the MOF surface, and (ii) the ability of CMC to adjust its shape to the surface of CALF-20 due to its flexible carboxymethyl groups. This hybrid material also exhibits a thermodynamic CO_2/N_2 selectivity equal to that of pristine CALF-20. Lastly, CMC shows no negative influence on CO_2 kinetics.

MOF composites have also been studied as potential candidates for SO_2 adsorption. ZIF-8, a material based on Zn and imidazolate ions, has shown promise in that regard, especially under humid conditions; unfortunately, its SO_2 sorption capacity is virtually non-existent at low RH. In contrast, CALF-20 has been proven to exhibit sufficient SO_2 uptake under dry conditions, but it failed at high RH. Therefore, Peterson *et al.* combined these two MOFs to form composite granules capable of SO_2 filtration across a wide range of humidities.[57]

The materials were mixed in varying ratios with poly(styrene-*block*-ethylene-*co*-butylene-*block*-styrene) (SEBS), an elastomeric polymer allowing for satisfactory diffusion of toxic gases. The phase inversion method was employed to develop the composite beads. Firstly, the performance of pure MOFs was examined at relative humidities ranging from 0 to 80%. As expected, the calculated SO_2 uptake under dry conditions was 1.7 mol kg^{-1} for CALF-20 and 0.2 mol kg^{-1} for ZIF-8, whereas the values at high RH changed to 0.1 mol kg^{-1} for CALF-20 and 5.1 kg mol^{-1} for ZIF-8. The analysis of the SO_2 desorption process on CALF-20 confirmed the physical nature of the adsorption. However, off-gassing of SO_2 resulted in a $\sim$20% loss of the surface area of this material. ZIF-8, in turn, was proven to chemically bind SO_2, leading to partial destruction of its structure. These tests were then followed by CO_2 and N_2 adsorption experiments on the composites. The surface area of the materials increased along with the increasing ZIF-8 content. The breakthrough tests at varying humidities revealed that the composite with a 50:50 MOF composition exhibits the best SO_2 filtration capacity.

The performance of CALF-20 in comparison to other MOFs

One of the key attributes of CALF-20 is its stability under humid conditions. It has also been proven to withstand exposure to steam at 150 °C.[18] The structure of the material remained unchanged even after soaking in water[25] or exposing to acid gases,[18] thereby matching or surpassing many benchmark MOFs,[58] including moisture-stable SIFSIX-2-Cu-i,[59] water-stable UiO-66,[60] or ZnF(daTZ), which remains stable in boiling water and at pH values ranging from 1 to 12.[61] Simultaneously, CALF-20 exhibits high CO_2 uptake compared to other materials. Under ambient conditions, it adsorbs 4.07 mmol g^{-1} of carbon dioxide. Although this is not the highest CO_2 sorption capacity reported to date, for instance, MAF-X25ox adsorbs 7.14 mmol g^{-1}.[62] CALF-20 still outperforms materials such as UiO-66-NH_2 (3 mmol g^{-1}),[63] IR-MOF-74-III-CH_3 (2.90 mmol g^{-1}),[64] or ZU-301 (2.44 mmol g^{-1}).[65]

Another material with a comparable CO_2 sorption capacity to that of CALF-20 is amine-functionalised Mg-MOF-74, which can be produced and structuralised on a large scale. This framework exhibits an interesting cooperative adsorption phenomenon,[66] adsorbing up to 4.1 mmol g^{-1} of CO_2 from a 15% CO_2-in-N_2 mixture saturated with water.[67] However, a two-step preparation process involving functionalisation and a decrease in diamine loading to 97% after only 1000 temperature swing adsorption cycles[68] makes this material inferior to CALF-20 in terms of its applicability.

The carbon dioxide uptake capacity of CALF-20 combined with its high CO_2/N_2 selectivity of 230 makes this framework an excellent CO_2 adsorbent. Even more importantly, the crystallinity of CALF-20 and its CO_2 sorption performance under humid conditions remain satisfactory, while most MOFs show structural instability in the presence of water. For example, HKUST-1 exhibits high CO_2 uptake and remains stable in

CO_2/N_2 separation processes after multiple TSA cycles,[69] but does not show long-term resistance to humidity.[70] On the other hand, ZIF-8, a promising CO_2 sorbent, was originally reported to display exceptional thermal and chemical stability, particularly in boiling water and alkaline solutions.[71] However, several studies have proven that hydrothermal conditions can trigger structural changes in this material or even lead to its hydrolysis.[72]

Another important aspect for the industrial applications of metal–organic frameworks is their scalability and production cost. Although materials such as ZIF-8, MIL-100(Fe), or HKUST-1 can be synthesised at a kilogram scale,[73] large-scale production of MOFs is still limited. Nevertheless, CALF-20 excels in this aspect: the multi-ton scalability of its synthesis has allowed it to be mass-produced by Svante.[25] This is widely regarded as one of the most successful implementations of a MOF under industrial conditions, primarily due to its economically beneficial synthetic route.[73]

Experimental and computational studies of CALF-20-related materials

The astounding success of CALF-20 in carbon capture technologies caused a surge of interest in the development of structurally related materials that could enhance various properties of this MOF. It turned out that a simple change in reaction medium may result in a successful production of a novel framework with new, potentially useful properties. An attempt to further reduce the synthesis cost of CALF-20 by using water as the only solvent unexpectedly led to the formation of its isomer, dubbed NCU-20 $[Zn_2(trz)_2(ox)\cdot 4H_2O]$ (Fig. 5a).[74] Although NCU-20 crystallises in the space group $P2_1/n$ and maintains the connectivity of its predecessor, slight changes in the geometry of its network reduce the channel aperture from 5.2×5.7 Å in CALF-20 to 4.2×4.7 Å in NCU-20. This adjustment enhances its capability for selective adsorption of propylene (C_3H_6) over propane (C_3H_8) (Fig. 5b). Single-component adsorption experiments revealed that NCU-20 can adsorb up to 94.41 cm^3 cm^{-3} of propylene at 1 bar and 298 K. This value is higher than that of any other C_3H_6/C_3H_8 sieving adsorbent to date. Fortunately, propane adsorption under the same conditions is negligible (6.12 cm^3 cm^{-3}). The C_3H_6/C_3H_8 selectivity at 0.5 bar, which corresponds to industrial conditions of propylene production, equals 22.2 and surpasses those of most other adsorbents. The applicability of NCU-20 for separation of propylene from propane was also tested using DCB experiments at high temperatures. The satisfactory difference between the breakthrough times of these two gases (~ 18 min g^{-1} at 353 K) combined with the ability to collect high-purity ($> 99.5\%$) propylene during the desorption process and the consistent separation performance of the adsorbent (confirmed after five sorption/regeneration cycles under both dry and humid conditions) indicates that NCU-20 is a promising candidate for C_3H_6/C_3H_8 separation. Furthermore, the stability of the material was verified after soaking it in room
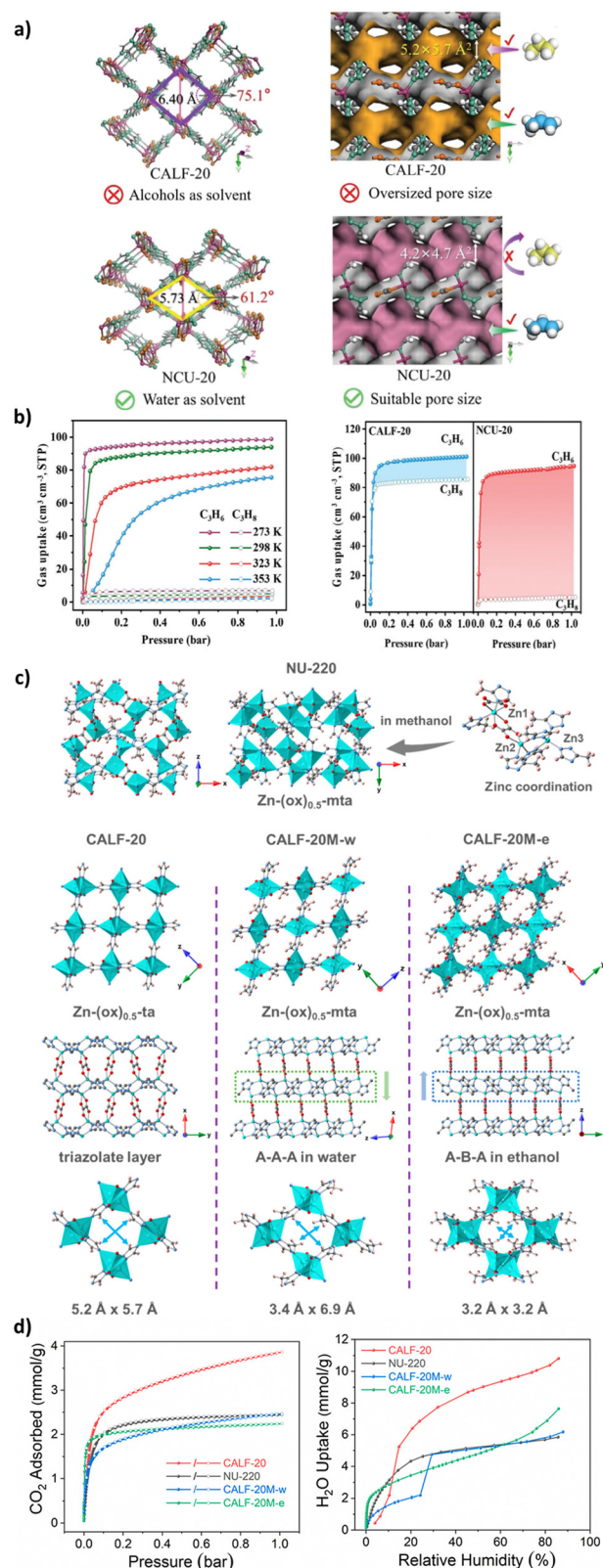

Fig. 5 (a) Comparison of channels in CALF-20 and NCU-20 along with (b) C_3H_6 and C_3H_8 isotherms on NCU-20 at 273–353 K (left); representation of differences between propylene/propane uptake in CALF-20 and NCU-20. Adapted with permission from ref. 74. Copyright 2024, Wiley. (c) Crystal structures of new $[Zn(mta)(ox)_{0.5}]$ frameworks and (d) their CO_2 (left) and water (right) isotherms at 298 K. Adapted with permission from ref. 75. Copyright 2024, ACS.

temperature water for eight months and in boiling water for two hours. Finally, the synthetic procedure is easily scalable and costs $10 per kg, compared to $30 per kg for CALF-20.[74]

The CO_2 sorption capacity of CALF-20 is hindered at relative humidity above 40%. Wang *et al.* aimed to increase the hydrophobicity of the framework by introducing a methyl group to the triazolate anion.[75] As a result, they obtained three new MOFs based on 3-methyl-1,2,4-triazole (mta) (Fig. 5c), with the product varying according to the solvent used during the reaction. Using water or ethanol led to the creation of two isostructural materials compared to CALF-20, called CALF-20M-w and CALF-20M-e, respectively. Both materials have the formula $[Zn(mta)(ox)_{0.5}]$, but they differ in terms of symmetry and the mutual arrangement of Zn-mta layers. The pore apertures in these materials (3.4×6.9 Å^2 in CALF-20M-w and 3.2×3.2 Å^2 in CALF-20M-e) are smaller than those in CALF-20 due to the presence of the methyl group attached to the mta ligand.

On the other hand, the synthesis in methanol yielded a novel material dubbed NU-220, whose formula is identical to those of the aforementioned materials. Notably, the framework displays the highest symmetry among all the MOFs reported by Wang and coworkers, crystallising in the tetragonal space group $P4_32_12$. It also features three distinct types of zinc cations, each with a different coordination number (ranging from 4 to 6) and varying compositions of the coordination sphere. Among the four materials discussed, CALF-20M-e demonstrates the highest CO_2 adsorption at low concentrations (Fig. 5d) as well as the highest heat of adsorption, indicating that it interacts with carbon dioxide more strongly than other MOFs. While all three new frameworks exhibit lower water uptake at higher relative humidities than CALF-20 (Fig. 5d), they adsorb more water at <10% RH, contrary to the intended outcome of the study. Nevertheless, the analysis of the CO_2 sorption capacities under humid conditions carried out based on DCB studies revealed that NU-220 can adsorb more carbon dioxide than CALF-20 at <30% RH, while CALF-20M-w and CALF-20M-e exhibit high uptake capacities at higher humidities, even retaining 20% of their initial capacity at 80% RH. These new materials outperformed CALF-20, which loses all CO_2 sorption capacity at 70% RH.

Standardised accelerated aging studies featuring a 15-day incubation of all three new MOFs at 343 K and 80% RH proved the increased stability of the new materials under high humidity conditions. Molecular simulations show that the presence of methyl groups decreases the likelihood of hydrogen bond network formation by water molecules, thus enhancing the humidity resistance of CALF-20M-w and CALF-20M-e. Conversely, immersing NU-220 and CALF-20M-e in water at 453 K led to irreversible phase transformations resulting in the formation of CALF-20M-w. All three materials exhibit high chemical stability, as evidenced by the retention of their crystallinity after exposure to acidic gases.

Five years before the first report on CALF-20, a microporous MOF composed of zinc, oxalate, and 3-amino-1,2,4-triazolate (Atz) with the formula of $[Zn_2(Atz)_2(ox)\cdot0.5H_2O]$, denoted as ZnAtzOx_MeOH, was shown to adsorb 4.35 mmol g^{-1} of CO_2 at 1.2 bar and 273 K, with stability proven over eight

adsorption–desorption cycles.[76] A series of topologically related MOFs obtained from the same reagents, but different solvents, was then reported by Banerjee *et al.*[77] The connectivity and symmetry of those phases were identical to those in ZnAtzOx_MeOH, though each displayed a different level of corrugation. Moreover, the CO_2 uptake of the phases synthesised in water and *n*-BuOH was higher than that for ZnAtzOx_MeOH, reaching 4.7 mmol g^{-1} at 1.1 bar and 293 K. A gate-opening mechanism was observed for these frameworks at 0.2 bar and 273 K, but shifted to 0.765 bar at 293 K. The material retained its uptake capacity even after sixteen sorption cycles. An immersion in boiling water for a week resulted in no significant loss of crystallinity and only a 6% decrease of its CO_2 sorption capacity. Nevertheless, the CO_2 sorption performance of the MOF in humid conditions has not been investigated.

Based on these findings, J. Peng and coworkers obtained ZnAtzOx from an H_2O/*n*-BuOH mixture in order to verify the ability of the framework to separate propane from propene.[44] Time-dependent adsorption profiles measured at 650 torr across a range of temperatures confirmed that this material adsorbs propene significantly faster than propane, exhibiting the highest selectivity at 323 K. However, the selectivity coefficient is notably lower for ZnAtzOx compared to CALF-20 (220 and 1565, respectively). Additionally, the authors confirmed the water and moisture stability of ZnAtzOx at room temperature: neither soaking the MOF for one week nor exposing it to humidity for two days triggered any changes to the powder patterns of the samples. However, the separation performance of ZnAtzOx in DCB experiments remains to be investigated.

ZnAtzOx was also tested as a potential separating agent for xenon/krypton mixtures.[47] Its Xe adsorption isotherms at 278–298 K reveal a pronounced step and significant hysteresis, suggesting the flexibility of the framework. The Xe/Kr selectivity was studied using DCB experiments, which confirmed that ZnAtzOx adsorbs Xe preferentially. However, the difference between the breakthrough times of both gases is only one minute, rendering this material unsuitable for separation purposes.

CALF-20 is an example of a framework consisting of pillared layers. A common way to adjust the pore aperture in such materials, therefore tuning their ability to accommodate different guest molecules, is the functionalisation of the so-called pillar ligand. An example of such an alteration is a computational analysis of a family of CALF-20-based MOFs where the oxalate ligand was replaced by squarate (Squ), fumarate, benzenedicarboxylate, thieno[3,2-*b*]thiophene-2,5-dicarboxylate, and cubanedicarboxylate ions.[78] The substitution of the linker was studied in light of its influence on the CO_2 sorption capability of the new frameworks over N_2 under varying humidity conditions. Binary mixture (CO_2 15:85 N_2) GCMC simulations revealed that SquCALF-20 shows the best performance at low CO_2 concentrations with selectivity surpassing 500 at 1 bar and 293 K, which is significantly higher than that for CALF-20 (180). In the presence of humidity, SquCALF-20 displays greater hydrophilicity, leading to higher H_2O uptake at low RH. However, this material still adsorbs more CO_2 than CALF-20 at 20% RH (3.4 mmol g^{-1} *vs.* 2.7 mmol g^{-1} for CALF-20).

Li *et al.* studied a series of isoreticular polymers built from Zn-aminotriazolate layers pillared by various 2-substituents of 1,4-benzene-dicarboxylate (bdc-x).[79] All six MOFs obtained have the formula of $[Zn(Atz)(bdc-x)_{0.5}]$. They are isostructural and crystallise in the tetragonal $P4/nnc$ space group. These materials contain two types of channels: a smaller, more hydrophobic one created between carbon backbones of the ligands, and a larger one, displaying a hydrophilic character due to the proximity of the amine groups in the triazolate ions. It is worth noting that, contrary to the oxalate ligand in CALF-20, which binds to the zinc centre using both oxygen atoms from each carboxylate moiety, the bdc linkers form only one coordination bond between the carboxylate and the metal ion. None of the reported materials adsorbs N_2 at 77 K. Only $[Zn(Atz)(bdc-CH_3)_{0.5}]$ and $[Zn(Atz)(bdc-NH_2)_{0.5}]$ exhibit CO_2 uptake at 195 K, as described by a type I isotherm. The latter MOF also demonstrates the highest acetylene uptake, reaching 25.3 cm^{-3} g^{-1} at 1 bar and 273 K, with the lowest heat of adsorption among all the materials. It has also been shown to have the highest affinity for water vapour in the series, due to its water sorption capacity at partial pressure below 0.1. However, the report lacks an analysis of the separation properties of the materials and the assessment of their stability and uptake capacity under humid conditions.

Perspectives and conclusions

The recent surge of interest in CALF-20 stems from its remarkable balance of properties, including stability, durability, processability, and high CO_2 selectivity in the presence of water. Its relatively low preparation cost, compared to other benchmark metal–organic frameworks for carbon capture and storage,[80,81] has led to an industrial application of this material in cement plants. This has driven the research community to study the chemistry of CALF-20 in greater detail.

However, some studies have highlighted that the major drawback of CALF-20 is its competitive adsorption of water, which limits its effectiveness at lower CO_2 concentrations and higher H_2O concentrations.[18,28] Nevertheless, experiments with preloaded CO_2 indicate that CALF-20 might be effective even in high humidity, where the CO_2 concentration is as low as 2%.[34] This finding underscores the need to assess the potential of CALF-20 in natural gas-fired electrical plants, where flue gas typically contains 3–5% CO_2 and 10–12% water. Given the scalability and stability of this material, the potential for utilising CALF-20 for CO_2 capture from flue gas in chimneys or from polluted city air should be investigated.

On the other hand, CALF-20 has already been proven to effectively separate components of cracking gas mixtures[45] and provide benchmark selectivity of butene isomers.[29,46] However, these properties have only been verified on a laboratory scale, highlighting the necessity to develop systems allowing for the employment of CALF-20 for separation purposes under industrial conditions.

Moreover, reports of certain aspects such as the mechanical and thermal properties of α-CALF-20[49] remain largely theoretical and require further experimental validation. For example, the predicted negative area compressibility, negative linear compressibility, and negative thermal expansion of α-CALF-20 should be investigated using varying pressure and temperature single-crystal or powder diffraction experiments. Computational studies have suggested transformations of α-CALF-20 into new, denser phases at high pressures[49] or very low temperatures,[25] which necessitates experimental verification.

Furthermore, the novel τ- and γ-CALF-20 phases, which incorporate water molecules attached to zinc cations and can be obtained as single crystals,[32] require analogous theoretical and experimental investigations. Since these phases are obtained after prolonged exposure of α-CALF-20 to elevated temperature, the effect of long-term heating of the material under industrial conditions should also be studied.

Finally, it is crucial to discover new materials with improved properties. Research indicates that CALF-20-related materials repeatedly exhibited superior sorption and selectivity capabilities, even under varying humidity conditions. Importantly, these materials are comparably cost-effective to produce as pure CALF-20.[74] We anticipate that they will soon become a key focus in the capture and separation of various gases. To facilitate the development of this area, computational chemists should investigate novel and existing MOFs inspired by the structural features of CALF-20, with particular emphasis on the identified guest/gas binding sites.[32] By adopting this approach, researchers could gain a better understanding of the feasibility and scalability of the CALF-20-related materials for practical/industrial applications. In addition to performance evaluations, these studies should also include comprehensive economic analyses of the components and synthetic processes involved.

In summary, it is essential to recognise that CALF-20 is an intriguing flexible MOF, which has already been produced on a large scale and widely utilised in CCS technologies. This material also shows potential for other gas-related applications. This report summarises significant advancements in the chemistry of CALF-20, providing a foundation for future studies aimed at accurately assessing the applicability of porous materials in addressing environmental challenges.

Abbreviations

ASU	Asymmetric unit
Atz	3-Amine-1,2,4-triazolate
bdc	1,4-Benzene-dicarboxylate
CCS	Carbon capture and storage
CMC	Carboxymethyl cellulose
CO_2RR	Electrocatalytic carbon dioxide reduction reaction
DCB	Dynamic column breakthrough
DFT	Density functional theory
GCMC	Grand canonical Monte Carlo
GO	Graphene oxide
IAST	Ideal adsorption solution theory

MD	Molecular dynamics
MLP-MD	Machine learning potential molecular dynamics
MMM	Mixed matrix membrane
mta	3-Methyl-1,2,4-triazolate
NAC	Negative area compressibility
NTE	Negative thermal expansion
ox	Oxalate
P-XRD	Powder X-ray diffraction
PGDE	Permselective gas diffusion electrode
PIM	Polymer of intrinsic porosity
RDF	Radial distribution function
RH	Relative humidity
RHE	Reversible hydrogen electrode
SC-XRD	Single-crystal X-ray diffraction
trz	Triazolate
TSA	Temperature swing adsorption

Author contributions

All authors prepared the review concept. KR and AJ wrote the abstract, introduction, perspectives and conclusions. JD conducted the literature research and wrote the remaining sections, as well as the initial draft. AJ and KR supervised the manuscript preparation and reviewed the final draft. All authors were actively involved in discussions regarding the organisation of the publication.

Data availability

No data were used for the research described in the article.

Conflicts of interest

There are no conflicts to declare.

Acknowledgements

Notes and references

1 G. T. Pecl, M. B. Araújo, J. D. Bell, J. Blanchard, T. C. Bonebrake, I.-C. Chen, T. D. Clark, R. K. Colwell, F. Danielsen, B. Evengård, L. Falconi, S. Ferrier, S. Frusher, R. A. Garcia, R. B. Griffis, A. J. Hobday, C. Janion-Scheepers, M. A. Jarzyna, S. Jennings, J. Lenoir, H. I. Linnetved, V. Y. Martin, P. C. McCormack, J. McDonald, N. J. Mitchell, T. Mustonen, J. M. Pandolfi, N. Pettorelli, E. Popova, S. A. Robinson, B. R. Scheffers, J. D. Shaw, C. J. B. Sorte, J. M. Strugnell, J. M. Sunday, M.-N. Tuanmu, A. Vergés, C. Villanueva, T. Wernberg, E. Wapstra and S. E. Williams, *Science*, 2017, **355**, eaai9214.

2 D. Breitburg, L. A. Levin, A. Oschlies, M. Grégoire, F. P. Chavez, D. J. Conley, V. Garçon, D. Gilbert, D. Gutiérrez, K. Isensee, G. S. Jacinto, K. E. Limburg, I. Montes, S. W. A. Naqvi, G. C. Pitcher, N. N. Rabalais, M. R. Roman, K. A. Rose, B. A. Seibel, M. Telszewski, M. Yasuhara and J. Zhang, *Science*, 2018, **359**, eaam7240.

3 R. E. Baker, A. S. Mahmud, I. F. Miller, M. Rajeev, F. Rasambainarivo, B. L. Rice, S. Takahashi, A. J. Tatem, C. E.

Wagner, L.-F. Wang, A. Wesolowski and C. J. E. Metcalf, *Nat. Rev. Microbiol.*, 2022, **20**, 193–205.

4 W. Steffen, J. Grinevald, P. Crutzen and J. McNeill, *Philos. Trans. R. Soc., A*, 2011, **369**, 842–867.

5 N. G. C. Change, Carbon Dioxide Concentration|NASA Global Climate Change, https://climate.nasa.gov/vital-signs/carbon-dioxide?intent=121, (accessed 7 October 2024).

6 CO2 Emissions in 2023 – Analysis, https://www.iea.org/reports/co2-emissions-in-2023, (accessed 7 October 2024).

7 T. R. Anderson, E. Hawkins and P. D. Jones, *Endeavour*, 2016, **40**, 178–187.

8 N. G. C. Change, Global Surface Temperature|NASA Global Climate Change, https://climate.nasa.gov/vital-signs/global-temperature?intent=121, (accessed 7 October 2024).

9 V. Ramanathan and Y. Feng, *Atmos. Environ.*, 2009, **43**, 37–50.

10 M. Springmann, M. Clark, D. Mason-D'Croz, K. Wiebe, B. L. Bodirsky, L. Lassaletta, W. de Vries, S. J. Vermeulen, M. Herrero, K. M. Carlson, M. Jonell, M. Troell, F. DeClerck, L. J. Gordon, R. Zurayk, P. Scarborough, M. Rayner, B. Loken, J. Fanzo, H. C. J. Godfray, D. Tilman, J. Rockström and W. Willett, *Nature*, 2018, **562**, 519–525.

11 A. Haines and K. Ebi, *N. Engl. J. Med.*, 2019, **380**, 263–273.

12 R. Cavicchioli, W. J. Ripple, K. N. Timmis, F. Azam, L. R. Bakken, M. Baylis, M. J. Behrenfeld, A. Boetius, P. W. Boyd, A. T. Classen, T. W. Crowther, R. Danovaro, C. M. Foreman, J. Huisman, D. A. Hutchins, J. K. Jansson, D. M. Karl, B. Koskella, D. B. Mark Welch, J. B. H. Martiny, M. A. Moran, V. J. Orphan, D. S. Reay, J. V. Remais, V. I. Rich, B. K. Singh, L. Y. Stein, F. J. Stewart, M. B. Sullivan, M. J. H. van Oppen, S. C. Weaver, E. A. Webb and N. S. Webster, *Nat. Rev. Microbiol.*, 2019, **17**, 569–586.

13 T. Terlouw, C. Bauer, L. Rosa and M. Mazzotti, *Energy Environ. Sci.*, 2021, **14**, 1701–1721.

14 M. Bui, C. S. Adjiman, A. Bardow, E. J. Anthony, A. Boston, S. Brown, P. S. Fennell, S. Fuss, A. Galindo, L. A. Hackett, J. P. Hallett, H. J. Herzog, G. Jackson, J. Kemper, S. Krevor, G. C. Maitland, M. Matuszewski, I. S. Metcalfe, C. Petit, G. Puxty, J. Reimer, D. M. Reiner, E. S. Rubin, S. A. Scott, N. Shah, B. Smit, J. P. M. Trusler, P. Webley, J. Wilcox and N. M. Dowell, *Energy Environ. Sci.*, 2018, **11**, 1062–1176.

15 M. Pardakhti, T. Jafari, Z. Tobin, B. Dutta, E. Moharreri, N. S. Shemshaki, S. Suib and R. Srivastava, *ACS Appl. Mater. Interfaces*, 2019, **11**, 34533–34559.

16 G. Singh, J. Lee, A. Karakoti, R. Bahadur, J. Yi, D. Zhao, K. AlBahily and A. Vinu, *Chem. Soc. Rev.*, 2020, **49**, 4360–4404.

17 M. Ding, R. W. Flaig, H.-L. Jiang and O. M. Yaghi, *Chem. Soc. Rev.*, 2019, **48**, 2783–2828.

18 J.-B. Lin, T. T. T. Nguyen, R. Vaidhyanathan, J. Burner, J. M. Taylor, H. Durekova, F. Akhtar, R. K. Mah, O. Ghaffari-Nik, S. Marx, N. Fylstra, S. S. Iremonger, K. W. Dawson, P. Sarkar, P. Hovington, A. Rajendran, T. K. Woo and G. K. H. Shimizu, *Science*, 2021, **374**, 1464–1469.

19 G. Ozin, CALF-20, https://www.advancedsciencenews.com/calf-20-a-carbon-capture-success-story/, (accessed 7 October 2024).

20 G. K. H. Shimizu, R. Vaidhyanathan, S. Iremonger, K. Deakin, J.-B. Lin and K. W. Dawson, *CA Pat.*, WO2014138878, 2014.

21 J. M. Taylor, R. K. Mah and G. K. H. Shimizu, *US Pat.*, 11230562B2, 2019.

22 X.-F. Wei, J. Miao and L.-L. Shi, *Synth. React. Inorg. Met.-Org. Chem.*, 2016, **46**, 365–369.

23 M. N. Corella-Ochoa, J. Benet-Buchholz, M. Martínez-Belmonte and J. R. Galán-Mascarós, *Inorg. Chem.*, 2015, **54**, 4678–4687.

24 Y. Higuchi, M. Sugita, S. Moriya, T. Takewaki and S. Tanaka, *Microporous Mesoporous Mater.*, 2024, **374**, 113137.

25 R. Oktavian, R. Goeminne, L. T. Glasby, P. Song, R. Huynh, O. T. Qazvini, O. Ghaffari-Nik, N. Masoumifard, J. L. Cordiner, P. Hovington, V. Van Speybroeck and P. Z. Moghadam, *Nat. Commun.*, 2024, **15**, 3898.

26 T. T. T. Nguyen, J.-B. Lin, G. K. H. Shimizu and A. Rajendran, *J. Chem. Eng.*, 2022, **442**, 136263.

27 R. Krishna and J. M. van Baten, *Sep. Purif. Technol.*, 2025, **352**, 128269.

28 T. T. T. Nguyen, B. M. Balasubramaniam, N. Fylstra, R. P. S. Huynh, G. K. H. Shimizu and A. Rajendran, *Ind. Eng. Chem. Res.*, 2024, **63**, 3265–3281.

29 Y.-P. Jiang, C. Deng, C.-X. Liang, X. Peng, Z. Zhang, L. Zhao, X.-C. Wu, J.-S. Zou, Y. Jia, M.-J. Cheng, J.-H. Li, J. Zhang, Y.-L. Peng, M. Gao, G.-J. Chen and M. J. Zaworotko, *ACS Mater. Lett.*, 2024, 4972–4979.

30 S. Roy, F. A. Philip, E. F. Oliveira, G. Singh, S. Joseph, R. M. Yadav, A. Adumbumkulath, S. Hassan, A. Khater, X. Wu, P. Bollini, A. Vinu, G. Shimizu, P. M. Ajayan, M. G. Kibria and M. M. Rahman, *Cell Rep.*, 2023, **4**, 101269.

31 Z. Chen, C.-H. Ho, X. Wang, S. M. Vornholt, T. M. Rayder, T. Islamoglu, O. K. Farha, F. Paesani and K. W. Chapman, *ACS Mater. Lett.*, 2023, 2942–2947.

32 J. Drwęska, F. Formalik, K. Roztocki, R. Q. Snurr, L. J. Barbour and A. M. Janiak, *Inorg. Chem.*, 2024, **63**, 19277–19286.

33 X. Wang, T. Zhao, Y. Cai, Y. Zheng, Y. Chen and J. Gao, *J. Solid State Chem.*, 2023, **327**, 124280.

34 J. Hastings, T. Lassitter, N. Fylstra, G. K. H. Shimizu and T. G. Glover, *Ind. Eng. Chem. Res.*, 2024, **63**, 11544–11551.

35 N. S. Wilkins, J. A. Sawada and A. Rajendran, *J. Chem. Eng. Data*, 2024, **69**, 1781–1803.

36 A. L. Sutton, M. Munir Sadiq, J. I. Mardel and M. R. Hill, *CrystEngComm*, 2024, **26**, 6003–6007.

37 M. Y. Borzehandani, M. N. Jorabchi, E. Abdulmalek, M. B. Abdul Rahman and M. A. Mohammad Latif, *Polymers*, 2023, **15**, 760.

38 A. Rajendran, G. K. H. Shimizu and T. K. Woo, *Adv. Mater.*, 2024, **36**, 2301730.

39 C.-H. Ho and F. Paesani, *ACS Appl. Mater. Interfaces*, 2023, **15**, 48287–48295.

40 Y. Magnin, E. Dirand, G. Maurin and P. L. Llewellyn, *ACS Appl. Nano Mater.*, 2023, **6**, 19963–19971.

41 R. Krishna and J. M. van Baten, *Sep. Purif. Technol.*, 2025, **355**, 129553.

42 T. T. T. Nguyen, G. K. H. Shimizu and A. Rajendran, *J. Chem. Eng.*, 2023, **452**, 139550.

43 S. B. Peh, D. Zhao, J. Jiang, S. Farooq and D. Zhao, *Chem. Eng. Sci.*, 2025, **301**, 120744.

44 J. Peng, H. Wang, D. H. Olson, Z. Li and J. Li, *Chem. Commun.*, 2017, **53**, 9332–9335.

45 X. Peng, L. Zhao, Y.-L. Peng, C. Deng, A. Y. Hjiej, H. Pan, Y.-J. Tian, J.-S. Zou, R. Krishna, B. Liu, C. Deng, P. Xiao, C. Sun, M. J. Zaworotko, G. Chen and Z. Zhang, *CCS Chem.*, 2024, **0**, 1–13.

46 Y.-T. Li, W. Li, L.-P. Zhang, S. Ni, Y. Jiang, X. Li and Q.-Y. Yang, *Adv. Funct. Mater.*, 2024, 2411951.

47 L. Yu, S. Xiong, Y. Lin, L. Li, J. Peng, W. Liu, X. Huang, H. Wang and J. Li, *Inorg. Chem.*, 2019, **58**, 15025–15028.

48 Y. Wei, F. Qi, Y. Li, X. Min, Q. Wang, J. Hu and T. Sun, *RSC Adv.*, 2022, **12**, 18224–18231.

49 D. Fan, S. Naskar and G. Maurin, *Nat. Commun.*, 2024, **15**, 3251.

50 Q. Jia, E. Lasseuguette, H. Kaur, A. B. Naden, M.-C. Ferrari and P. A. Wright, *Chem. Commun.*, 2024, **60**, 11128–11131.

51 H. Zhang, L. Sheng, J. Chen, X. Wang, P. Tao, D. Ren, H. Cui, K. Yang, Z. Tang, Z. Zhang, X. He and H. Xu, *Carbon Capture Sci. Technol.*, 2024, **13**, 100276.

52 T. A. Al-Attas, N. N. Marei, X. Yong, N. G. Yasri, V. Thangadurai, G. Shimizu, S. Siahrostami and M. G. Kibria, *ACS Catal.*, 2021, **11**, 7350–7357.

53 T. Al-Attas, S. K. Nabil, A. S. Zeraati, H. S. Shiran, T. Alkayyali, M. Zargartalebi, T. Tran, N. N. Marei, Md. A. Al Bari, H. Lin, S. Roy, P. M. Ajayan, D. Sinton, G. Shimizu and M. G. Kibria, *ACS Energy Lett.*, 2023, **8**, 107–115.

54 W. Feng, K. Liu, J. Liu, J. Jin, J. Mi, S. Xu and H. Meng, *Sep. Purif. Technol.*, 2024, **343**, 127102.

55 M. Sedighi, M. J. Azarhoosh, H. Alamgholiloo and N. N. Pesyan, *Process Saf. Environ. Prot.*, 2024, **190**, 1481–1493.

56 S. Naskar, D. Fan, A. Ghoufi and G. Maurin, *Chem. Sci.*, 2023, **14**, 10435–10445.

57 G. W. Peterson, L. Mundy, T. M. Tovar, X. Wang and O. K. Farha, *ACS Appl. Eng. Mater.*, 2024, **2**, 2295–2301.

58 C. Xiao, J. Tian, Q. Chen and M. Hong, *Chem. Sci.*, 2024, **15**, 1570–1610.

59 P. Nugent, Y. Belmabkhout, S. D. Burd, A. J. Cairns, R. Luebke, K. Forrest, T. Pham, S. Ma, B. Space, L. Wojtas, M. Eddaoudi and M. J. Zaworotko, *Nature*, 2013, **495**, 80–84.

60 J. H. Cavka, S. Jakobsen, U. Olsbye, N. Guillou, C. Lamberti, S. Bordiga and K. P. Lillerud, *J. Am. Chem. Soc.*, 2008, **130**, 13850–13851.

61 Z. Shi, Y. Tao, J. Wu, C. Zhang, H. He, L. Long, Y. Lee, T. Li and Y.-B. Zhang, *J. Am. Chem. Soc.*, 2020, **142**, 2750–2754.

62 P.-Q. Liao, H. Chen, D.-D. Zhou, S.-Y. Liu, C.-T. He, Z. Rui, H. Ji, J.-P. Zhang and X.-M. Chen, *Energy Environ. Sci.*, 2015, **8**, 1011–1016.

63 G. E. Cmarik, M. Kim, S. M. Cohen and K. S. Walton, *Langmuir*, 2012, **28**, 15606–15613.

64 A. M. Fracaroli, H. Furukawa, M. Suzuki, M. Dodd, S. Okajima, F. Gándara, J. A. Reimer and O. M. Yaghi, *J. Am. Chem. Soc.*, 2014, **136**, 8863–8866.

65 C. Yu, Q. Ding, J. Hu, Q. Wang, X. Cui and H. Xing, *Chem. Eng. J.*, 2021, **405**, 126937.

66 T. M. McDonald, J. A. Mason, X. Kong, E. D. Bloch, D. Gygi, A. Dani, V. Crocellà, F. Giordanino, S. O. Odoh, W. S. Drisdell, B. Vlaisavljevich, A. L. Dzubak, R. Poloni, S. K. Schnell, N. Planas, K. Lee, T. Pascal, L. F. Wan, D. Prendergast, J. B. Neaton, B. Smit, J. B. Kortright, L. Gagliardi, S. Bordiga, J. A. Reimer and J. R. Long, *Nature*, 2015, **519**, 303–308.

67 J. A. Mason, T. M. McDonald, T.-H. Bae, J. E. Bachman, K. Sumida, J. J. Dutton, S. S. Kaye and J. R. Long, *J. Am. Chem. Soc.*, 2015, **137**, 4787–4803.

68 P. J. Milner, R. L. Siegelman, A. C. Forse, M. I. Gonzalez, T. Runčevski, J. D. Martell, J. A. Reimer and J. R. Long, *J. Am. Chem. Soc.*, 2017, **139**, 13541–13553.

69 S. Ye, X. Jiang, L.-W. Ruan, B. Liu, Y.-M. Wang, J.-F. Zhu and L.-G. Qiu, *Microporous Mesoporous Mater.*, 2013, **179**, 191–197.

70 J. B. DeCoste, G. W. Peterson, B. J. Schindler, K. L. Killops, M. A. Browe and J. J. Mahle, *J. Mater. Chem. A*, 2013, **1**, 11922–11932.

71 K. S. Park, Z. Ni, A. P. Côté, J. Y. Choi, R. Huang, F. J. Uribe-Romo, H. K. Chae, M. O'Keeffe and O. M. Yaghi, *Proc. Natl. Acad. Sci. U. S. A.*, 2006, **103**, 10186–10191.

72 S. Tanaka and Y. Tanaka, *ACS Omega*, 2019, **4**, 19905–19912.

73 D. Chakraborty, A. Yurdusen, G. Mouchaham, F. Nouar and C. Serre, *Adv. Funct. Mater.*, 2024, **34**, 2309089.

74 Z. Deng, L. Yang, H. Xiong, J. Liu, X. Liu, Z. Zhou, S. Chen, Y. Wang, H. Wang, J. Chen, S. Deng, B. Chen and J. Wang, *Small Methods*, 2024, 2400838.

75 X. Wang, M. Alzayer, A. J. Shih, S. Bose, H. Xie, S. M. Vornholt, C. D. Malliakas, H. Alhashem, F. Joodaki, S. Marzouk, G. Xiong, M. Del Campo, P. Le Magueres, F. Formalik, D. Sengupta, K. B. Idrees, K. Ma, Y. Chen, K. O. Kirlikovali, T. Islamoglu, K. W. Chapman, R. Q. Snurr and O. K. Farha, *J. Am. Chem. Soc.*, 2024, **146**, 3943–3954.

76 R. Vaidhyanathan, S. S. Iremonger, K. W. Dawson and G. K. H. Shimizu, *Chem. Commun.*, 2009, 5230–5232.

77 A. Banerjee, S. Nandi, P. Nasa and R. Vaidhyanathan, *Chem. Commun.*, 2016, **52**, 1851–1854.

78 K. Gopalsamy, D. Fan, S. Naskar, Y. Magnin and G. Maurin, *ACS Appl. Eng. Mater.*, 2024, **2**, 96–103.

79 X.-Y. Li, H.-Y. Duan and C. He, *Inorg. Chem.*, 2022, **61**, 17634–17640.

80 K. Sumida, D. L. Rogow, J. A. Mason, T. M. McDonald, E. D. Bloch, Z. R. Herm, T.-H. Bae and J. R. Long, *Chem. Rev.*, 2012, **112**, 724–781.

81 P. M. Bhatt, Y. Belmabkhout, A. Cadiau, K. Adil, O. Shekhah, A. Shkurenko, L. J. Barbour and M. Eddaoudi, *J. Am. Chem. Soc.*, 2016, **138**, 9301–9307.